



Synchrotron radiography and tomography of water transport in perforated gas diffusion media

J. Haußmann ^{a,*}, H. Markötter ^b, R. Alink ^c, A. Bauder ^d, K. Dittmann ^b, I. Manke ^b, J. Scholta ^a

^a Zentrum für Sonnenenergie und Wasserstoff-Forschung Baden-Württemberg (ZSW), Helmholtzstr. 8, 89081 Ulm, Germany

^b Helmholtz-Zentrum Berlin für Materialien und Energie (HZB), Hahn-Meitner-Platz 1, 14109 Berlin, Germany

^c Fraunhofer Institute for Solar Energy Systems (ISE), Heidenhofstrasse 2, 79110 Freiburg, Germany

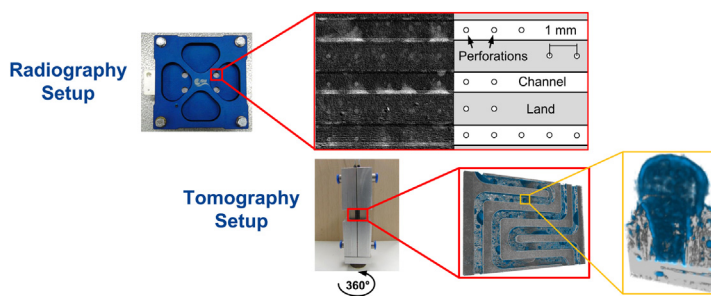
^d German Aerospace Center (DLR), Pfaffenwaldring 38-40, 70569 Stuttgart, Germany



HIGHLIGHTS

- Micro porous layer cracks proved to transport liquid water.
- Laser perforation of micro porous layer enhanced water transport just slightly.
- Improved water transport is found for complete gas diffusion media perforations.
- Highest performance is achieved for perforations with 60 μm of diameter.
- Synchrotron tomography shows water filling behavior of different perforations.

GRAPHICAL ABSTRACT



ARTICLE INFO

Article history:

Received 1 October 2012

Received in revised form

3 February 2013

Accepted 6 February 2013

Available online 16 February 2013

Keywords:

PEM fuel cell

Gas diffusion layer perforation

Micro porous layer crack

Water transport

Synchrotron X-ray imaging

ABSTRACT

Water transport in gas diffusion media (GDM) is investigated by synchrotron radiography and tomography. It is demonstrated that micro porous layer (MPL) cracks improve the water management in polymer electrolyte membrane (PEM) fuel cells. A further treatment by means of laser perforation is expected to enhance this effect. The radiography analysis reveals that water transport is practically not influenced by perforations applied only to the MPL. In contrast, perforations through the whole GDM (including the MPL) have a strong influence on the overall water transport behavior and are therefore considered for a deeper analysis. Performance measurements show a correlation between the perforation size and the fuel cell power density. An optimum is found for a perforation diameter of 60 μm . Synchrotron tomography analysis reveals that this optimum is due to an improved draining effect on the area around the perforation. Moreover, SEM and EDX analysis show a loss of PTFE on the GDM surface in the vicinity of the perforation due to the laser processing. The tomography images reveal water accumulations in this area that can be explained by the hydrophilic surface.

© 2013 Elsevier B.V. All rights reserved.

1. Introduction

One of the main issues of polymer electrolyte membrane fuel cells is the water discharge of product water [1]. By optimizing the water transport in the gas diffusion layer and the micro porous layer, respectively, gas diffusion in the porous structure is

* Corresponding author. Tel.: +49 731 9530 209; fax: +49 731 9530 666.

E-mail address: jan.haussmann@zsw-bw.de (J. Haußmann).

enhanced. This allows a better performance also under critical operation conditions [2–5].

There are many possible ways to improve the gas diffusion medium (GDMs) which consists of the gas diffusion layer (GDL) and the micro porous layer (MPL). The morphology and the composition of the fiber substrate (namely the GDL) and the micro porous material are influencing the surface properties of the material and thus the water accumulation and transport. A more specific understanding of the morphology can be achieved by analyzing treated GDM materials.

Commercial gas diffusion media with micro porous layers show cracks on the MPL surface. As reported from Lu et al. [6] these cracks might serve as initial water transport paths. This was also proven with in-situ measurements of water transport through MPL cracks using soft X-rays by Sasabe et al. [7] and by quasi-in-situ synchrotron tomography by Markötter et al. [8].

Using this idea of initial water transport ways, a further optimization of the porous structure with artificial treatment of GDL and MPL is expected to enhance the water transport. Already Knights et al. [9], Kimball et al. [10] and Nishida et al. [11] analyzed the performance of mechanically perforated and grooved gas diffusion media, respectively. With each concept an enhanced water transport and a performance increase under certain conditions is supposed.

One different concept is using laser processing for adding perforations throughout the whole porous material. This concept was first performed by Gerteisen et al. [12] with a neodymium doped garnet laser system. In an untreated Toray TGP-H-090 gas diffusion medium without MPL, laser perforations with 80 μm in diameter have been added. Single Cell and fuel cell stack tests revealed an enhanced performance for perforated GDM material [13]. Different humidification conditions and perforation sizes were related to performance and investigated with impedance spectroscopy by Manahan et al. [14,15]. In these studies an SGL Sigracet® 10 BB material is perforated with an ytterbium fiber laser and the perforation sizes 100 μm and 300 μm are analyzed. A deeper investigation of the water distribution of perforations has been performed [14], in which neutron imaging technique is used to distinguish influences of perforations on the different regions of the flow field. Previous studies of Hartnig et al. [16] and Manke et al. [17,18] already showed a good detectability of liquid water for in-situ radiographic measurements and quasi-in-situ tomography. As neutron imaging is limited in its resolution and water transport within the GDM is only roughly detectable [19–25], other imaging techniques are more advantageous. Alink et al. [26] was realizing high resolution visualization of water transport in laser perforated GDM using an ex-situ SEM setup. The first in-situ synchrotron measurements of perforated GDM were later performed by Markötter et al. [27], in which water transport through a perforated Toray TGP-H-090 without MPL has been investigated.

Besides synchrotron radiography tomography plays a more important role as its advantage is the local resolved detection of water within the porous materials [28–35]. Krüger et al. [36] designed a single fuel cell for synchrotron tomography measurements which revealed the water distribution in the single-meander flow field and the gas diffusion medium. Further studies of Markötter et al. [8,37] revealed water transport ways through the porous material. However, a differentiation of water and carbon fibers was not achieved. Eller et al. [38] solved this problem by subtracting the tomogram of the operated cell from the tomogram of the dry cell. Thus, the 3D water information was separated and by combination with the dry cell tomogram the water distribution in the GDM could be analyzed.

In this paper, in-situ synchrotron measurements continued concentrating on laser perforation of commercial GDMs with MPL

for comparison with untreated material. In addition, first synchrotron tomography experiments reveal the filling behavior of perforations with difference in size and are compared with the latest performance measurements.

2. Experimental

2.1. Material treatment with laser perforation technique

Laser perforation has advantages compared to other perforation techniques, like milling, drilling or graving. Since it is not a mechanical process the material can be treated much faster. A Neodymium doped Yttrium Aluminum Garnet (Nd:YAG) laser was chosen as a suitable laser system which has already been used in previous experiments by Gerteisen et al. [12,13]. With an ultra-short pulsed laser (Trumpf TruMicro Series) perforations in gas diffusion media have been manufactured in air atmosphere down to a diameter of 30 μm.

Perforation of GDM materials with laser processing is possible, because components of these materials are mainly carbon, PTFE and a polymeric binder which can be removed due to the heat impact of the laser beam. The pulse duration of the laser system can be set to the nanosecond scale, so that the heat transfer to the surroundings of the perforated material is reduced. To achieve different perforation sizes either the power and total laser impact time is adjusted or by moving the specimen in a circle of appropriate diameter. In these experiments, perforation sizes between 30 μm and 400 μm have been processed and analyzed. By adding perforations with 30 μm of diameter the pore structure of the fiber substrate is not influenced, because most of the pore sizes are in the same order of magnitude. Basically the morphology of the MPL is modified. The small perforation size is chosen to be similar to the size of the MPL cracks. Instead, perforations with 400 μm of diameter are changing the morphology of the fiber substrate, as well. These large pathways inserted into the whole GDM are directly connecting the catalyst layer and the flow field channel facilitating water transport. Additionally, perforation sizes of 60, 80 and 150 μm are analyzed to find a performance optimum in perforation diameter. The results are shown in the following chapters.

As a GDM material the commercial Sigracet® 25 BC from SGL (25 BC) has been chosen. The GDL is equipped with an MPL which shows MPL cracks on the surface. For a better understanding of the function of MPL cracks an additional treatment of the MPL is planned. Since with the laser perforation technique a separate treatment of GDL and MPL is not possible, this issue has been solved by separately manufacturing MPLs using the dry deposition technique. This process has been developed by Gülow et al. [39] and had been adapted to manufacture MPLs with a comparable composition as the MPL of commercial 25 BC material.

This MPL was first processed by the laser perforation technique and afterwards combined with the Sigracet® 25 BA from SGL which is the same GDL substrate as the one of the 25 BC. Thus, a comparison between separately combined porous layers and the commercial material is possible. The main material parameters are listed in Table 1.

Table 1
Material properties of the deployed GDM, GDL and MPL.

	SGL 25 BC	SGL 25 BA	Dry-sprayed MPL
Thickness Substrate (μm)	190 ^a	190 ^a	
Thickness MPL (μm)	45 ^a (additional)		40
PTFE-content (wt. %)	5 ^a (substrate)	5 ^a	20

^a Manufacturer value.

The laser perforated material is employed only on the cathode side. An enhanced water transport is more promising on this side, because performance decrease due to liquid water blockage and the resulting insufficient oxygen concentration is more pronounced at the cathode side than on the anode side. Hence, GDM laser perforation for the anode is not discussed here.

2.2. Synchrotron imaging

Synchrotron visualization is a suitable tool for analysis of water transport and distribution in PEM fuel cells. The high spatial resolution of down to $2 \mu\text{m} \text{ pixel}^{-1}$ allows the detection of water in the fiber substrate of the GDL.

During the experiments two different setups were chosen. On the one hand the radiography setup for in-situ analysis of dynamic water transport was used which has been successfully tested by Markötter et al. [27]. On the other hand the tomography setup was applied for a detailed water distribution analysis based on quasi-in-situ measurements developed by Krüger et al. [36]. For both setups a different fuel cell design has been developed (Fig. 1). Each design is made to get the most realistic representation of water transport and distribution inside a running fuel cell, respectively. But the designs are also adapted to the boundary conditions of synchrotron imaging. In the visualized area all materials with a high attenuation coefficient for X-rays (metals, e.g. Aluminum) are spared out or exchanged with a less attenuating material (e.g. polycarbonate).

The radiography and tomography measurements have been carried out at the beam line “BAMline” at the Synchrotron “BESSY II” in Berlin, see Ref. [40]. With both fuel cell setups synchrotron beam energies between 15 and 20 keV were chosen. A double multilayer monochromator selects an energy with a resolution of $\Delta E/E = 1.5\%$. The X-ray beam is transmitted through the fuel cell and projecting the cell information onto a scintillator screen which is imaged onto a CCD camera with a resolution of 4008×2672 pixel (Fig. 2). The fuel cells for the radiography and tomography measurements are exposed by the synchrotron beam for not more than 1 h and 3 h, respectively. Due to the beam attenuation of the fuel cell materials, mainly the platinum particles, an additional heat of about 2 mW cm^{-2} is generated at the catalyst layer. A reduction in cell voltage or other degradation phenomena as reported from Refs. [41,42] were not observed in these measurements.

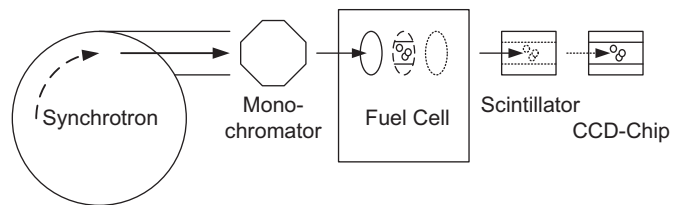


Fig. 2. Synchrotron imaging setup showing the beam of electrons (---), X-rays (-) and photons (...) with the main components of the beam line.

2.2.1. Synchrotron radiography

For the in-situ analysis of liquid water transport inside a PEM fuel cell, synchrotron radiography serves as a valuable tool to benefit from both, a good time resolution and a high spatial resolution. Water transport dynamics with a time interval of 5 s/image were recorded with a resolution of $2.2 \mu\text{m} \text{ pixel}^{-1}$ and a limited visualized area of $8.8 \times 5.9 \text{ mm}^2$.

In order to analyze water transport mechanisms in a realistic fuel cell setup, a standard fuel cell (ZSW) with an active area of 100 cm^2 was used. To achieve high synchrotron beam transmission in the field of view, cut-outs with a diameter of 10 mm have been arranged in the aluminium end plates. In these spots graphite composite backing plates have been reduced in material thickness to about 1 mm. In total four cut-outs have been installed in the fuel cell. Each cut-out is showing a part of the flow field from top-view (Fig. 3). This delivers the so called “through-plane-view”. The recorded images have been normalized with respect to the dry cell image to gain the water distribution, only. The water depth d in each radiographic image is calculated according to Lambert–Beer's law with intensity I and attenuation coefficient of water μ as $d = (\ln I - \ln I_0)/\mu$.

Information of the anode and cathode side is superimposed, but water droplet movements can be distinguished due to the opposite gas flow direction.

As a flow field a three-fold meander was chosen in which the gas velocity in each channel is rather high with standard gas stoichiometries. Average gas velocities per channel are about 17 m s^{-1} for air and 4 m s^{-1} for hydrogen. Thus, water droplets in the channel are quickly discharged and cannot superimpose the information of the water distribution in the GDM.

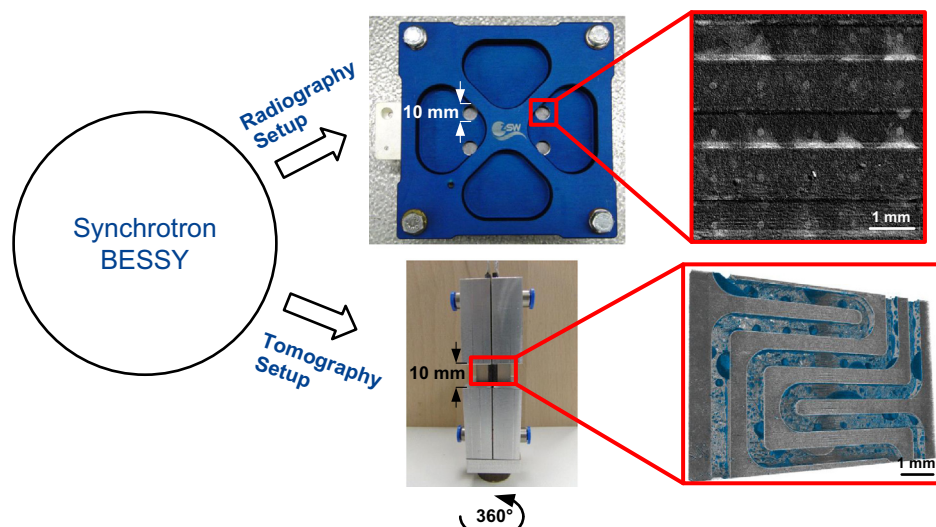


Fig. 1. Synchrotron radiography and tomography setup with exemplary images of the water distribution inside the fuel cell.

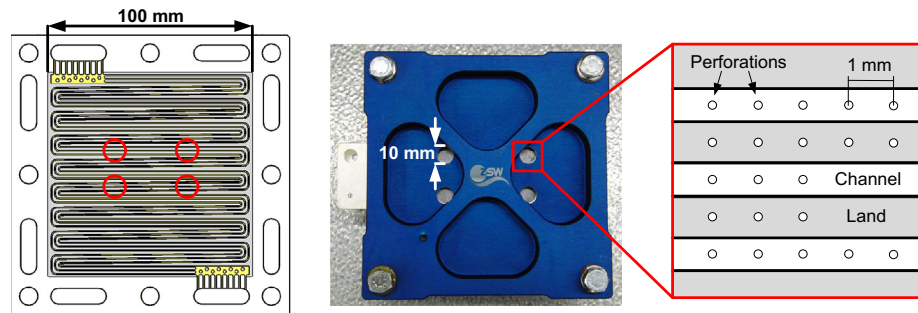


Fig. 3. Adapted fuel cell for synchrotron radiography with cut-outs and corresponding positions in the flow field (red circles) as well as perforation positions in channel and land area (red square). (For interpretation of the references to color in this figure legend, the reader is referred to the web version of this article.)

In all through-plane radiography experiments hydrogen flow was set to 1 l min^{-1} and air flow was set to 4 l min^{-1} which corresponds to a stoichiometry of 2.5 on the anode and 5 on the cathode at a current density of 0.5 A cm^{-2} . Gases were fully humidified at a temperature of 50°C .

The Membrane Electrode Assembly (MEA) in all experiments is a Gore™ Primea® series with a membrane thickness of $18 \mu\text{m}$. Treated gas diffusion media for the cathode side were aligned so that perforations appear in the middle of the channel and the land, respectively. On the anode side the standard 25 BC material was employed. Laser perforations in the radiographic experiments were all set to a diameter of $150 \mu\text{m}$, so that a comparison between the different GDL materials independent to the perforation size is possible.

2.2.2. Synchrotron tomography

Whereas synchrotron radiography can only show 2D information of the water distribution in fuel cells, synchrotron tomography

reveals in detail the positions of water accumulations in each layer [43,44]. Thus, a thorough analysis of the water balance is possible.

A previous study [36] showed the water distribution in a small fuel cell. The fuel cell had been operated under constant operating conditions and was stopped to obtain a representative water distribution. Afterwards the temperature regulation has been switched off to cool down the fuel cell to ambient temperature to avoid movements during the tomography. This procedure has been successfully tested by neutron radiography and tomography studies [45]. It is not expected that this general behavior is changing with the fuel cell setup or by using synchrotron radiation. Thus, water movements are not expected for the period of the tomography. Furthermore, the amount of condensing water is estimated to be negligible with the recorded resolution. Hence, neither water movements, nor water condensation are influencing the water distribution in the fuel cell, so that a representative condition can be analyzed.

For all tomography experiments the fuel cell has been rotated 360° scanning half of the visualized area of the fuel cell,

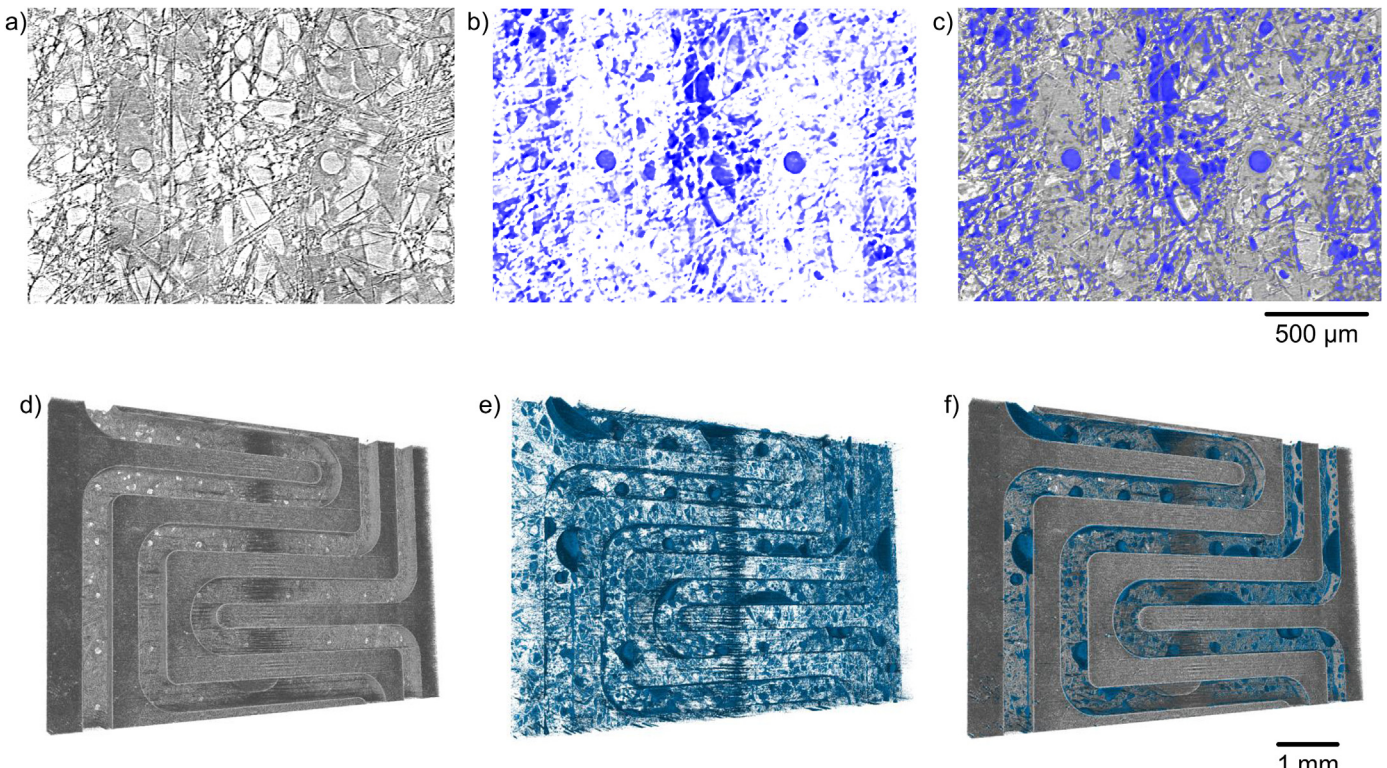


Fig. 4. Tomography images of the dry fuel cell (a), the water distribution (b) and the combined information of water accumulations inside the fuel cell (c) with $150 \mu\text{m}$ GDL-MPL perforations after 30 min of operation at 0.5 A cm^{-2} .

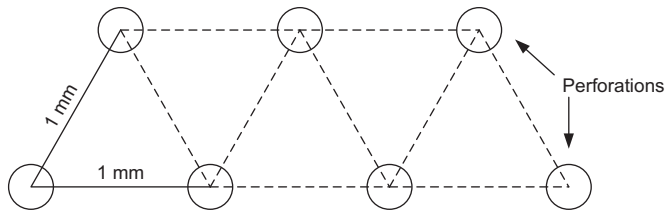


Fig. 5. Perforation pattern for the gas diffusion media which have been employed on the cathode side of the fuel cell for the performance tests.

$8.8 \times 5.9 \text{ mm}^2$. Due to the full rotation in the parallel beam the necessary information for the tomography are recorded. The reconstructed volume has the dimension of $17 \times 17 \times 5.9 \text{ mm}^3$. The pixel size was $4.3 \mu\text{m}$, so that small water clusters in the fibrous structure could be identified. But a differentiation between water and carbon fibers is not directly possible due to the similar X-ray attenuation of both materials at the relevant energies.

However, it was possible to differentiate between water and carbon fibers in these experiments. This has been achieved by an additional tomogram of the dry cell and later subtracting this cell information from the tomogram of the operated cell. Thus, only the 3D information of water is left and can be combined with the 3D information of the dry cell. Fig. 4 shows an example of this method. In these experiments this method has been successfully applied for the whole cell volume. It has been proven as a suitable tool for characterizing the influence of perforations on the water distribution.

For comparison with the radiography measurements the tomography setup is equipped with a three-fold meander flow field, as well. In these measurements gas flows were set to 0.3 l min^{-1} of hydrogen on the anode side and 0.7 l min^{-1} of air on the cathode side which corresponds to a stoichiometry of 15 on both sides at a current density of 0.5 A cm^{-2} . Gases were fully humidified at a temperature of 70°C .

In the tomography experiments laser perforations were added to the different layers and the perforation size was varied. The treated gas diffusion medium was employed on the cathode side

and the untreated 25 BC material on the anode side. The processed layer was aligned to the flow field, so that perforations are positioned in the middle of the each channel.

2.3. Performance measurements

For the characterization of perforations a performance analysis is necessary. If perforations are improving the water transport of PEM fuel cells, a performance change will be observed. For testing the treated materials a standard single fuel cell setup (ZSW) with an active area of 100 cm^2 comparable to the one for radiographic measurements was chosen. For analyzing low and high current densities optimized flow fields for anode and cathode side with each 23 meanders were used. The perforated materials have been employed on the cathode side and the untreated material (25 BC) on the anode side. In these measurements the perforations were set in a pattern which is independent from the flow field design. The distance of the perforations was set to 1 mm resulting in an equilateral triangle pattern (Fig. 5). As it was mentioned in Section 2.1 the perforation diameter was varied from $30 \mu\text{m}$ to $400 \mu\text{m}$ for the performance measurements. Operation conditions in the performance tests were set to fully humidified gases at 50°C with gas stoichiometries of 1.25 for hydrogen on the anode and 4 for air on the cathode.

2.4. EDX analysis

Scanning electron microscopy (SEM) and energy dispersive X-ray spectroscopy (EDX) have been chosen to be useful tools for analyzing laser perforated materials. It is assumed that effects from the laser perforation process on the material can occur, because high temperatures can easily affect material transformation or decomposition.

As it was shown in other works [14] a heat affected zone can be related with the laser processing. In these experiments perforations were scanned in different modes of the SEM using a standard secondary electron detector (SE) and a back scattered electron detector (BS). Further analysis of the surrounding of the perforation was achieved by EDX analysis. The main surface components have

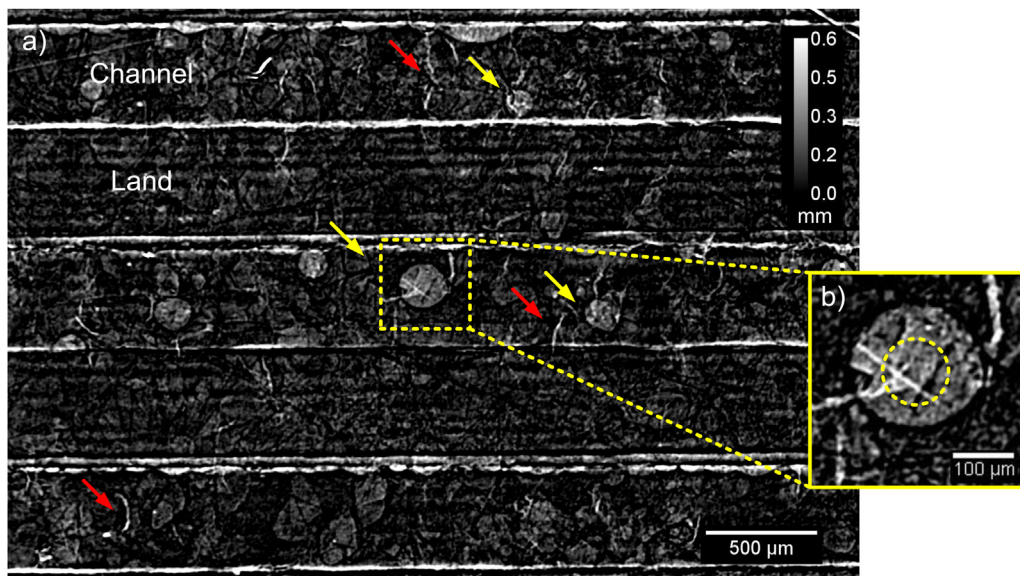


Fig. 6. The radiographic image shows the water depth distribution in mm of three channels and two lands after running the fuel cell for 6 min at 1 A cm^{-2} (a). It reveals no water transport ways for smaller MPL cracks (red arrows), but water bubble formations for bigger cracks (yellow arrows). One bigger MPL crack is zoomed (b) and the water fluctuation is analyzed inside the marked circle. (For interpretation of the references to color in this figure legend, the reader is referred to the web version of this article.)

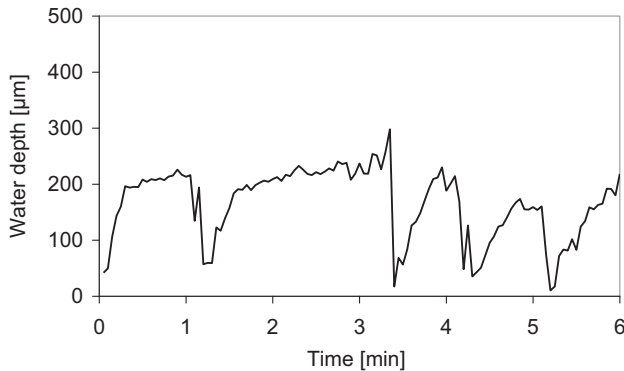


Fig. 7. Fluctuating water depth of the marked circle in Fig. 5 showing the water transport through the MPL crack from start-up of the fuel cell till 6 min of operation.

been identified and EDX maps were recorded. Results are helpful for comparison with the tomography results of the in-situ experiments. If a heat affected zone can be found which is influencing the water distribution, it will be revealed by synchrotron tomography analysis.

3. Results

3.1. Radiography results

3.1.1. Micro porous layer cracks

As a first result it is observed that cracks in the micro porous layer are playing a crucial role for the water transport. These cracks

are not only filling up first with liquid water, but are the origin of water transport ways through the porous structure of the GDM.

Fig. 5 shows an example of MPL cracks in a commercial Sigracet® 25 BC GDL from SGL which are filling up with water under a load of 1 A cm^{-2} at 100% relative humidity and 50°C cell temperature after 6 min of operation. The water path is very pronounced due to the fact that water droplets are forming at the interface between carbon fiber substrate and the gas channel. Especially bigger cracks are forming water paths (see yellow arrows Fig. 6a) whereas smaller cracks cannot be identified as an origin of water accumulation in the porous media (see red arrows Fig. 6a). Cracks which formed water transport paths to the channel were identified to be on the cathode side due to the discharge direction of the water droplets. The gas supply is arranged in cross flow mode, so that a correlation is possible.

To analyze the water transport behavior of these cracks, one of the bigger MPL cracks, where a transport effect is expected, is chosen (Fig. 6b). The radiographic images of this cut-out are recorded as described in Section 2.2.1 and the mean water depth is calculated inside the marked circle with a diameter of $100 \mu\text{m}$ of each image and plotted versus time (Fig. 7). Water droplets are forming inside the channel, growing up and discharged by passing water. This process is continuously repeating after a certain time. In the diagram (Fig. 7) the droplet formation and discharge is plotted for 6 min under steady state conditions. In this period of time the droplet formation and discharge process is repeating five times. The interval of each repetition differs between 54 and 126 s.

On the other hand, if MPL cracks are sited under the land, no water transport effect can be observed. Since MPL cracks differ in length and width and are irregularly and randomly distributed

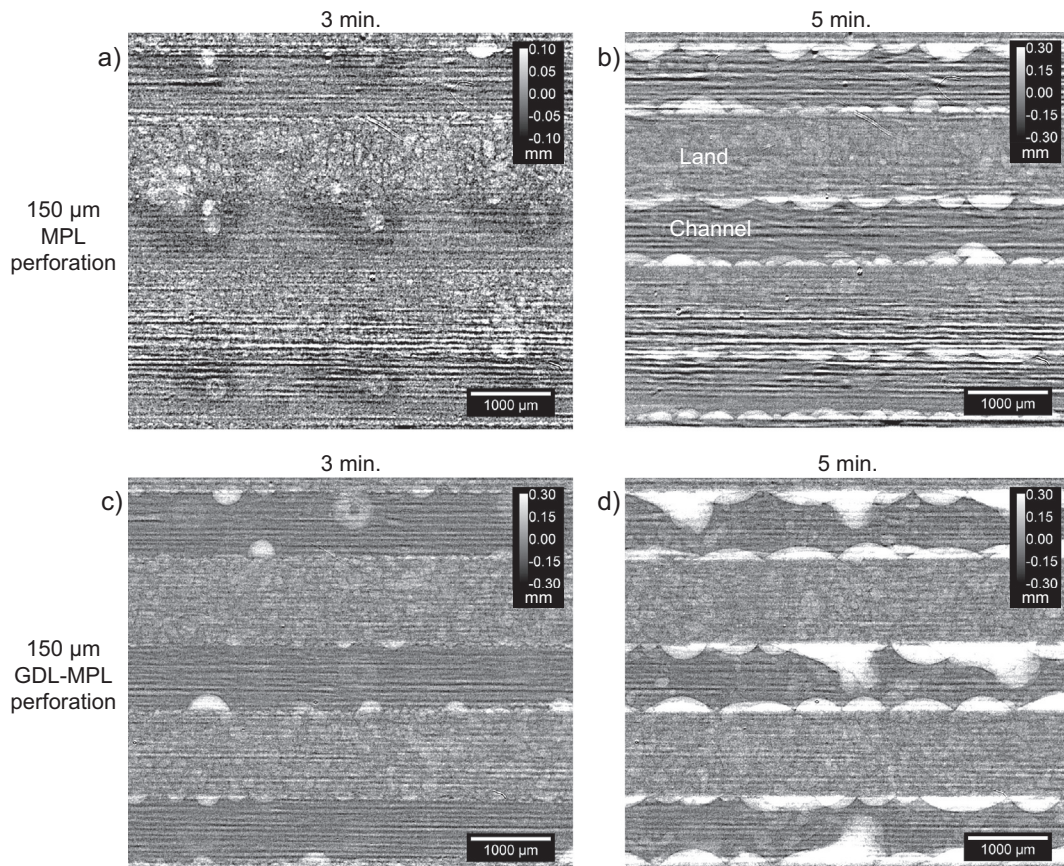


Fig. 8. The water depth distribution in mm of the radiographic images is shown 3 min and 5 min after start of fuel cell operation at 0.5 A cm^{-2} for MPL perforations (a, b) and for GDL-MPL perforations (c, d).

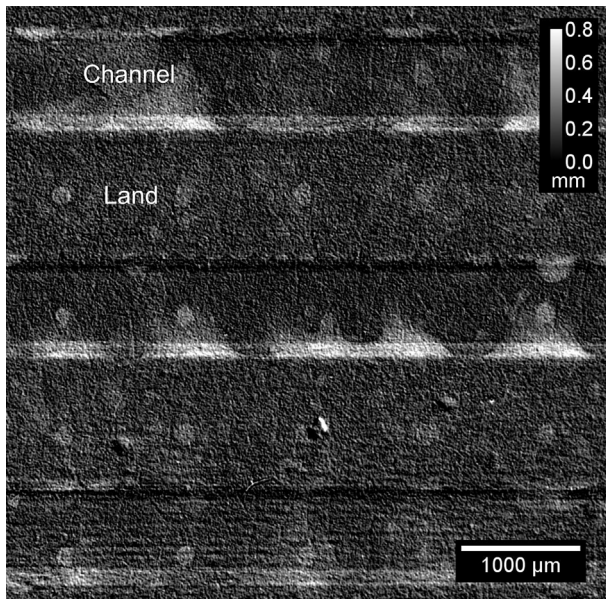


Fig. 9. The radiographic image reveals the water depth distribution in mm inside and around the perforated gas diffusion medium SGL Sigracet® 25 BC in the channel and the land region after 17 min of operation at 0.5 A cm^{-2} .

(Fig. 6a), only a limited effect of these cracks on the water transport is observed. Thus, artificial treatment of GDM materials in the channel area is expected to further enhance this liquid water transport effect.

3.1.2. Micro porous layer perforation

As a first experiment, an artificial treatment of the micro porous layer is accomplished. In order to manufacture pore paths which have an appropriate size for water transport, laser perforation has been chosen as a useful processing technique. MPL perforations have a diameter of 150 μm and are set in the middle of the channel with a distance of 2 mm to each other.

The radiography experiment reveals the effect of MPL perforations during start-up. As it is shown in Fig. 8a, the water distribution after 3 min of operation is clearly influenced by the artificial treatment. In the area of the perforation itself a higher water thickness (white) is measured, but in the surrounding less water accumulation (black) can be determined. Thus, water seems to be drained from the surroundings to the perforation.

A deeper analysis of the image reveals that the vicinity of the perforation is always covered by liquid water whereas it is continuously appearing and disappearing inside the perforations. The water appearance in the vicinity of the perforation can be related to the influence of the laser process which can make the material more hydrophilic. The fluctuations in the perforations instead are an indication for water transport through the perforations.

Hence, during start-up of the fuel cell, these perforations are influencing the water transport. But 5 min after operation (Fig. 8b) this effect is not more pronounced, but is covered by the overall water transport in the gas diffusion medium. Thus, influences of the artificial MPL perforation on the water management are playing only a minor part under these fully humidified conditions.

3.1.3. Micro porous layer and gas diffusion layer perforation

As a second experiment, the separate micro porous layer and the gas diffusion layer (SGL Sigracet® 25 BA) are combined and

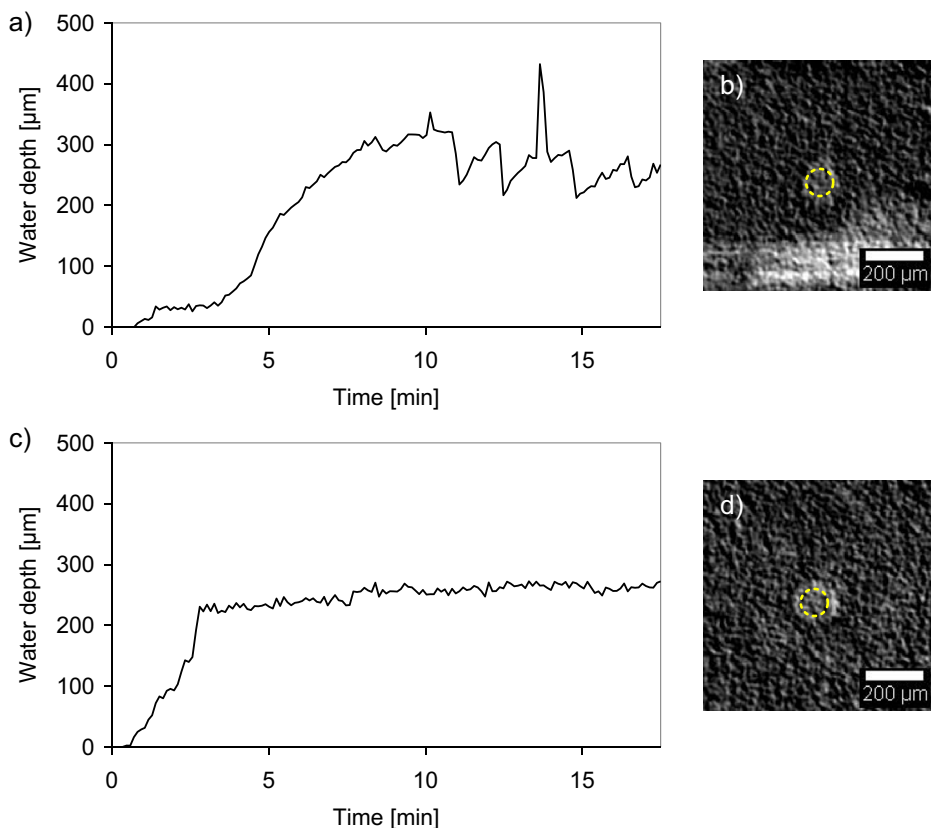


Fig. 10. The two plots show a strong water fluctuation characteristic for the perforation in the channel region (a) and a stable water depth for the perforation in the land region (c). The water depth has been calculated for the shown yellow circle (b, d) (diameter: 100 μm) of a representative perforation of Fig. 8. (For interpretation of the references to color in this figure legend, the reader is referred to the web version of this article.)

perforated afterwards by laser processing. Radiographies are taken for comparison with the previous results of the MPL perforations. The images of Fig. 8c and d are showing the water distribution three and 5 min after start of operation, respectively.

Right after start-up, water is accumulating in the vicinity of the perforations whereas the perforations themselves are kept water-free till 3 min of operation (Fig. 8c). Thus, the effect of the laser processing on the vicinity of the perforations is the same as with MPL perforations. On the contrary an explicit draining of water from the surroundings cannot be identified and a continuous change in the water depth is also not yet observed.

While the water transport effect with solely MPL perforation is not changing after 5 min, the effect is increasing with a complete MPL and GDL perforation (Fig. 8d). Perforations are filling up with water and a water path to the channel is build up. Thus, water preferably accumulates at the perforated regions in the channel. The water depth in these regions is fluctuating which is indicating water transport. Hence, the complete perforation of the gas diffusion medium seems preferable for an improved water management.

3.1.4. Gas diffusion medium perforation

In the first (3.1.2) and the second radiography experiments (3.1.3) of perforated porous layers, the water filling effect has been distinguished between perforation of the micro porous layer and perforation of the gas diffusion layer with added micro porous layer. Now, the perforation technique is adapted to commercially available GDM materials. For comparison with the radiographic analysis of MPL cracks (3.1.1) the same GDL material is chosen (SGL Sigracet® 25 BC). Additionally to the previous experiments (3.1.2, 3.1.3) which were focused on perforations set in the channel area, here the effect of perforations in the land area is analyzed, as well.

Radiographies are recorded from start-up under constant fuel cell operation conditions. After 17 min of operation perforations in the channel as well as under the land are visible (Fig. 9). Qualitatively, the filling behavior is similar to the one of the complete perforation of GDL and MPL (3.1.3), but the vicinity of the perforations is not visibly influenced and a higher water amount cannot be observed.

Influences on the overall water transport can be identified only in the channel region due to the forming of water accumulations around the perforations. Such an accumulation effect is not found for perforations under the land, because these water paths are a dead end, so that further water transport is strongly restricted.

For the analysis of time-dependent water transport radiographies are recorded from start-up till 17 min after start of operation. In Fig. 10a and b the mean water depth is calculated for the perforated area in the channel and under the land, respectively. The area is defined as a circle with a diameter of 100 μm as it is shown in Fig. 10c and d for each perforation.

The two diagrams reveal that in both regions first the perforation is filling up with water. Under the land the filling is finished within 3 min whereas in the channel area the complete filling takes about 8 min which already indicates an enhanced water discharge. After the filling process under the land the water content is stable at 230–270 μm of water depth. On the contrary the water content in the channel area is fluctuating significantly. It changes continuously between 320 and 210 μm. Also, during each cycle, a decrease in the water depth is observed initially, followed by a slow increase. The interval for each cycle is estimated to 84–138 s. Additionally, two peaks in the diagram show events of water droplets passing this part of the channel. This is not necessarily correlated with drawing water from the perforations. As it is shown in the diagram (Fig. 9a), the water depth before and after the peak are almost the same.

The continuous change in the water depth is a proof for water transport related to the perforations. Since perforations strongly influence the water transport in gas diffusion media, optimized perforation sizes might influence the performance of a fuel cell, as well.

3.2. Performance analysis

For the performance characterization of perforated gas diffusion media a single fuel cell has been set up as described in Section 2.3. From the results of the radiographic experiments (3.1) it is concluded that perforation of the complete gas diffusion medium is the most promising perforation technique. Besides, the perforation of commercially available GDMs allows a good comparison with the untreated material (3.1.1). Thus, only the commercial Sigracet® 25 BC GDL from SGL was perforated and tested for the performance measurements.

A polarization curve was recorded for each fuel cell setup which was equipped with a different perforated GDM (Fig. 11a). Differences in the performance are more pronounced for higher current densities. At a current density of 1.6 A cm⁻² all fuel cells equipped with perforated gas diffusion media show a higher voltage than the unperforated material. But the higher the perforation diameter the lower the performance increase. With 400 μm perforations an improved performance is not found until 1.2 A cm⁻². In contrast the fuel cell with 60 μm perforations already showed a positive effect at low current densities. Perforations which are much lower in diameter seem to lose this positive effect. The fuel cell equipped with 30 μm laser perforated GDM already showed a decrease in performance compared to the GDM with 60 μm perforations, but still exhibited a better performance than the reference GDM without perforations.

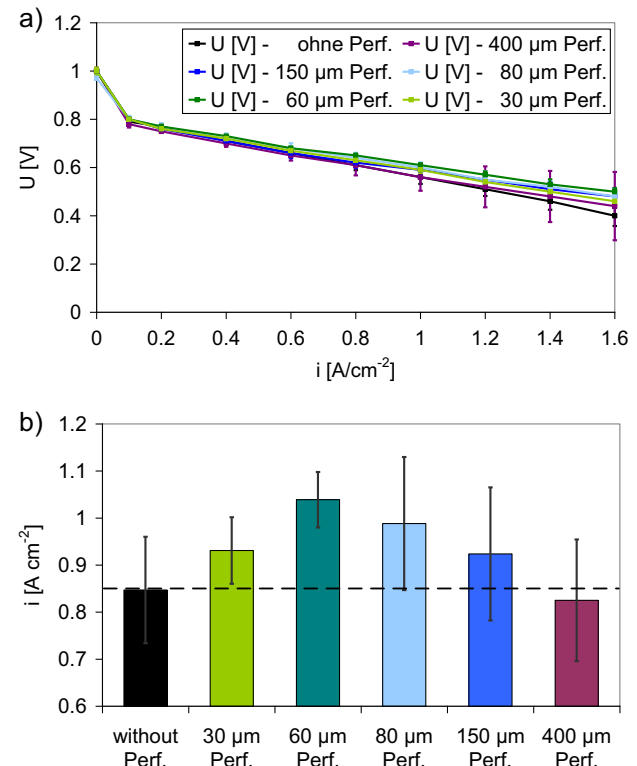


Fig. 11. Performance measurements of a 100 cm² test cell operated with fully humidified gases at 50 °C showing the polarization curves for the reference without perforation and the different perforation sizes (a). The corresponding current densities for 0.6 V (b) reveal a maximum in performance for 60 μm perforations.

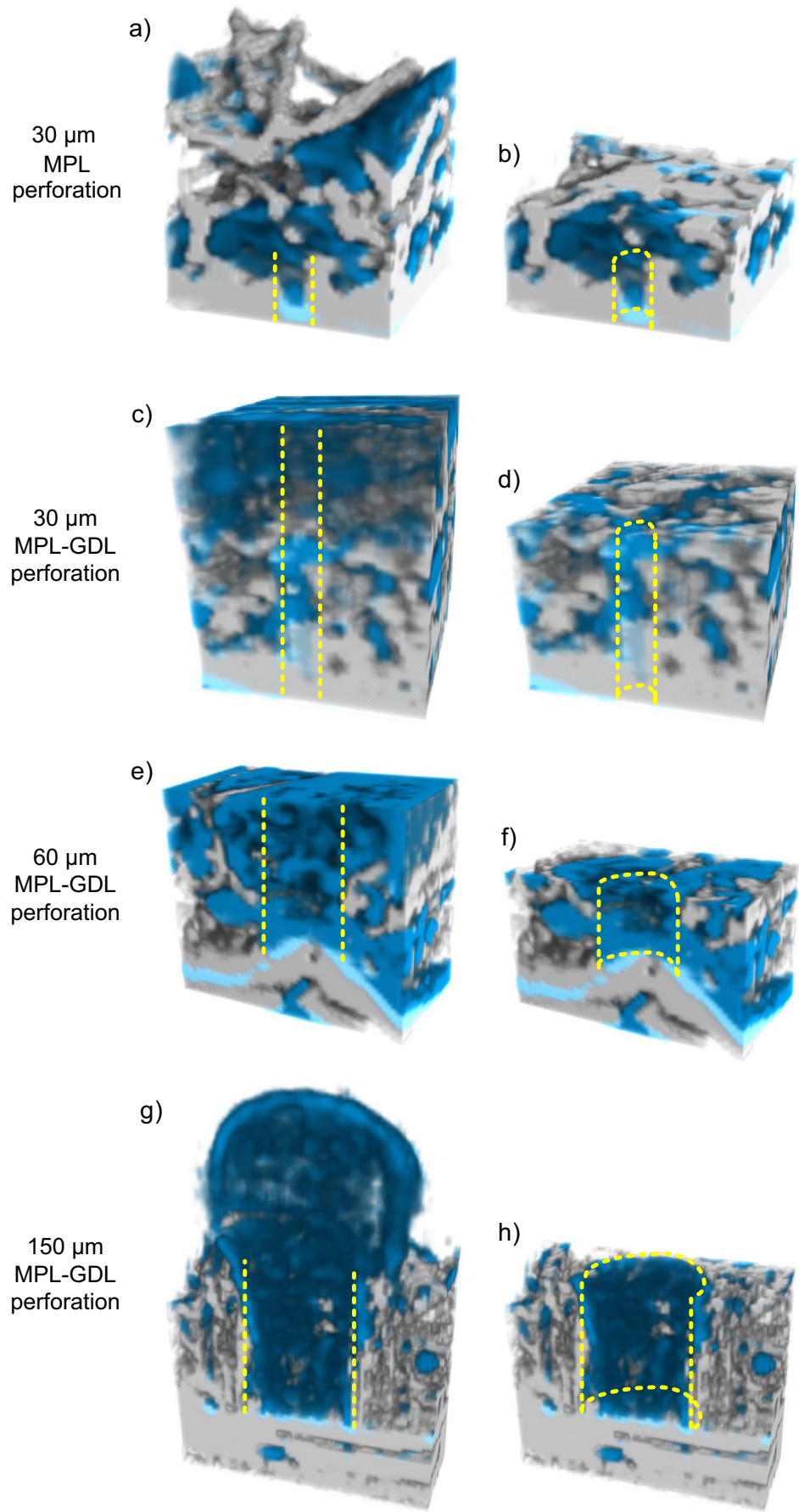


Fig. 12. Cut-outs are shown from tomography measurements in full-view and cross-sectional view with the water formation inside and around the artificial perforations after 30 min of fuel cell operation at 0.5 A cm^{-2} . Whereas 30 µm MPL (a, b) and MPL-GDL perforations (c, d) are influencing the water transport slightly, MPL-GDL perforations with 60 µm (e, f) and 150 µm (g, h) of diameter show a pronounced water path through the porous material.

For a more precise comparison the current density at a constant voltage is measured. In Fig. 11, the current densities for all five perforation sizes and the reference cell without perforation are compared at a voltage of 0.6 V to reveal the change in performance at a test point, relevant for fuel cell applications. Except for the perforation with 400 μm diameter, the performance of the fuel cell equipped with perforated GDMs increased. The trend in the diagram shows more precisely that with decreasing perforation diameter the performance of the fuel cell is increasing. The maximum performance (1.04 A cm^{-2} @ 0.6 V) is achieved with a perforation diameter of 60 μm . This corresponds to an increase of 23% compared with the reference material. On the other hand, a further decrease of the perforation size is already decreasing the performance again. Perforations with 30 μm of diameter exhibited the same current density as 150 μm perforations.

As the perforation size has been the only variable the water transport has to be improved due to the added perforations. For understanding the reason in the performance difference a deeper analysis of the filling behavior of the perforations is necessary. Synchrotron tomography of small fuel cells (2.2.2) equipped with perforated GDMs of different perforation sizes can help to understand this correlation.

3.3. Tomography results

The tomography images reveal in detail the filling behavior of the different perforations. Within the tomography experiments the difference between MPL- and MPL-GDL-perforation as well as the difference in the perforation sizes 30 μm , 60 μm and 150 μm are analyzed. For all tomography experiments the same setup and the same operation conditions as described in Section 2.2.2 are used. As an example in Fig. 4 the full tomogram of the 150 μm MPL-GDL perforations is shown in which the corresponding cut-out was found (Fig. 12g and h).

In Fig. 12 all four cut-outs are shown in full-view and half-cut-view to reveal the water distribution in all three dimensions. Comparing the filling between a 30 μm MPL-perforation (Fig. 12a and b) and a 30 μm MPL-GDL-perforation (Fig. 12c and d) no strong water transport effect is observable. In case of the MPL perforation water is appearing inside the perforation. The existing accumulation is not connected to the surface of the GDL in the channel area, but is spread in-plane. In case of the MPL-GDL perforation the artificial pore is water-free in the MPL region, but a part of the perforation in the GDL region is filled with water. In both cases no influence can be attributed to the water formation close to the GDL/channel interface.

Comparing the 30 μm GDL-MPL perforation with the bigger perforation sizes (60 μm , 150 μm) reveals that the filling behavior is not the same for the bigger perforations. In Fig. 12e–h the perforation is mostly filled with liquid water. In case of the perforation with 150 μm of diameter (Fig. 12g and h) also a droplet is forming on the surface to the channel. Such droplets have also been observed in the radiographic investigations of perforated 25BC material (Fig. 9).

Due to the complete filling of the 150 μm perforation, water transport is only slightly enhanced. Water which is produced close to the perforation tends to accumulate with the water inside the artificial pore. Thus, the water amount in the perforation is increasing and a water droplet is forming at the interface to the channel. This droplet grows till it is discharged into the channel. In the surrounding of the 150 μm perforation no water is visible which is draining into the perforation. Thus, the influence of this perforation is only concentrated on the area nearby and the performance increase is small.

In case of the perforation with 60 μm of diameter the artificial pore is also filled with liquid water, but the water is spreading in all

directions. Water is draining from the surroundings to the artificial pore and water is discharged into the channel in the same time (Fig. 12f). The perforation diameter is thereby bigger than the 30 μm perforation in which the draining effect is too weak. The perforation is also not too large as in case of the 150 μm perforation, in which the whole perforation is just filled with liquid water. Consequently, the 60 μm pore is showing an optimum between draining effect and filling behavior. Thus, an enhanced water transport through the pore is generated. This result is in line with the performance measurements of 3.2 in which the 60 μm perforation showed the highest power density.

Besides, the tomography measurements also show the influence of the laser perforation on the porous material. Fig. 13 shows as an example a slice of the tomogram for a 30 μm GDM perforation. The liquid water (red arrow) is visible which is accumulating around the perforation (yellow arrow). The diameter of this water attracted zone is about 250 μm . As this accumulation might be related to the laser process, EDX analysis can help to reveal the reason for the surface change of the material.

3.4. EDX analysis

SEM images and EDX scans were taken of the perforated GDM material with 30 μm of diameter as described in Section 2.4. Whereas in the SEM image with the secondary electron (SE) detector a surface change of the material around the perforation is not visible (Fig. 14a), the SEM image with the back scattered electron (BS) detector reveals the influence zone of the laser perforation process (Fig. 14b). In addition, Fig. 14c and d shows the EDX scans for carbon and fluorine of the perforated area, respectively. An area can be detected in which the fluorine concentration on the surface is decreased whereas the carbon concentration is increased. The reason for the change in material properties is mainly found in the high temperature influence of the laser process. In the influenced region the fluorine content of the surface is decreased from about 23 wt. % to about 14 wt. % in the close surrounding (white circle in Fig. 14b) and almost 0 wt. % in the main influence region. Carbon as the only other main component is therefore increased in its content from 77 wt. % to 86 wt. % and 100 wt. %, respectively. Fluorine is part of PTFE which is added to the carbon compound to make it hydrophobic. Due to the absence of fluorine the material surface is getting more hydrophilic and water can preferably accumulate in this area.

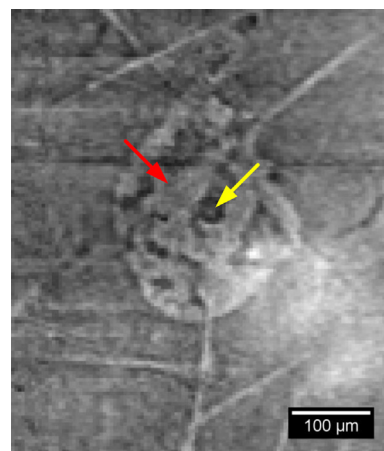


Fig. 13. Slice of a tomogram showing water accumulation (red arrow) around a 30 μm perforation (yellow arrow) which can be correlated with the heat affected zone (Fig. 13). (For interpretation of the references to color in this figure legend, the reader is referred to the web version of this article.)

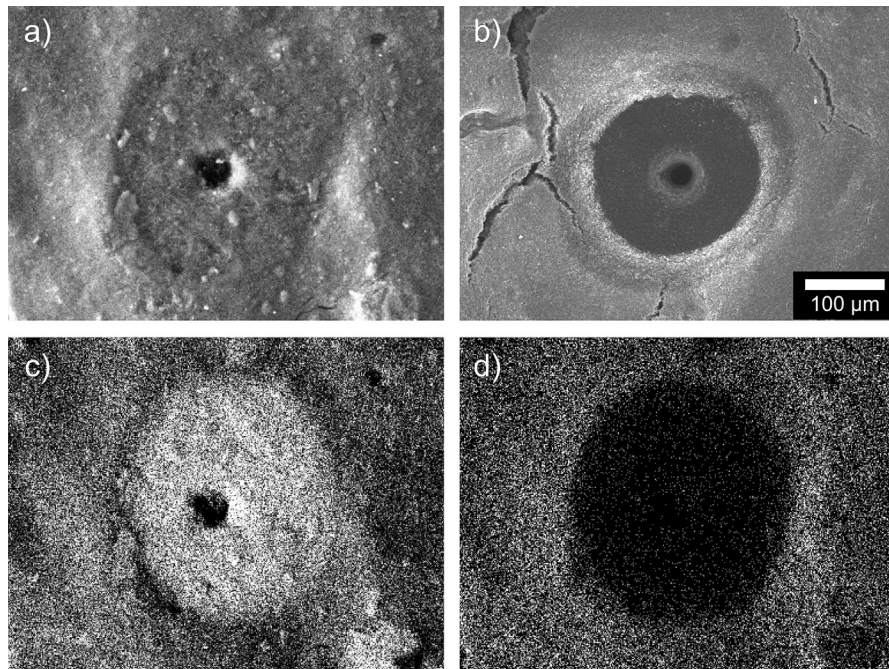


Fig. 14. SEM images show the heat affected zone around laser perforations with 30 μm of diameter, imaged with SE-detector (a) and BS-detector (b). EDX mapping of carbon (c) and fluorine (d) reveal the absence of flour in this zone due to the heat impact of the laser.

In the BS and EDX images the zone of influence is about 200–300 μm in diameter. This is the same geometry as it is observed for the water accumulation around the 30 μm perforation in the tomogram (Fig. 13). Thus, water is accumulating strongly around the perforated area due to the hydrophilic surface. Hence, a correlation between the change in material surface and the water accumulation around the perforation is proven.

This heat affected zone has about the same diameter for all analyzed perforation sizes. This means: the smaller the perforation size, the higher the influence of the heat affected zone. Thus, with small perforation sizes the water distribution is basically forming due to the change in material surface. Instead: the larger the perforation size, the smaller the heat affected zone. As a consequence, with larger perforation sizes the water distribution is influenced by the modified morphology. A deeper analysis of its influence on the water balance will be of interest for further studies.

4. Discussion

The water transport is improved by laser perforating a gas diffusion medium on the cathode side. A correlation between the perforation size and the performance increase has been achieved and as an optimum a perforation diameter of 60 μm has been found. The performance measurements have been set up using a pattern which is independent from the flow field geometry. Due to the results of the synchrotron radiography (3.1.2–3.1.4) which revealed a stronger water transport effect for perforations in the channel area a more enhanced water transport is expected for a flow field dependent perforation pattern.

A further performance increase is expected, if the amount of perforations per area is optimized. The distance in this investigation is set to 1 mm, but an increase of the perforation density might enhance the water discharge per area, as well.

Another important investigation would be the determination of the influence of perforations on lifetime. Due to the removal of the

micro porous layer in the perforated area the Membrane Electrode Assembly has no contact to the gas diffusion medium. This results in a lowered electrical and thermal conductivity. Higher ohmic losses are not observed in the polarization curves of perforated GDMs. Nonetheless, higher temperature gradients in the perforation areas might lead to higher degradation rates and fuel cell performance decreases with the time. Besides, the loss of mechanical compression in these areas is resulting in a deformation of the membrane. The tomography results reveal that the flexible membrane can bend inside the perforations (Fig. 12e and f). The mechanical stress of the membrane and the electrode as well as the loose contact to the next layers on the cathode and anode side might decrease long time stability. It is expected that the membrane bending is higher for larger perforation diameter. Thus, perforations with 150 μm of diameter should show a higher membrane bending in the perforated area, but this is not observed (Fig. 12g and h). A further analysis on this behavior will be discussed in future.

Finally, these measurements were showing precisely the preferred water transport ways through the gas diffusion medium. It is proven that artificial water transport pathways which are perpendicular to the layer structure of a PEM fuel cell can strongly enhance the water transport in these layers and thereby the performance of the fuel cell.

5. Conclusion

In this study water transport in gas diffusion media was investigated by synchrotron imaging. Synchrotron radiography measurements revealed that micro porous layer cracks can serve as water transport ways to the channel, if the crack size is sufficient and if it is located in the channel area of the flow field.

For a deeper understanding of water transport in these cracks, artificial perforations have been added to the porous material with laser processing. To differentiate the effect of the MPL and the GDL substrate, separate micro porous layers were manufactured. These

MPLs are first laser perforated and then combined with a GDL substrate. A comparison with the full perforated layers revealed a minor water transport effect for MPL perforations, but an enhanced effect for the complete perforation of MPL-GDL combinations and commercial GDM materials with MPL.

The latter were analyzed further by means of performance analysis in a standard single fuel cell. The variation of perforation diameter revealed a correlation between a decrease in perforation size and an increase in performance with an optimum diameter of 60 µm for the investigated GDM. A further decrease of perforation diameter resulted in a lowered performance. Compared to the untreated material a performance increase of 23% has been achieved.

Further investigations with synchrotron tomography showed the filling behavior of the analyzed perforations. Whereas small perforation sizes have a poor draining effect on the surroundings, large perforation sizes are filling up with water and water transport is only slightly improved. Optimized perforation sizes instead show a strong draining effect and an enhanced water transport till the GDM/channel interface.

Furthermore, water accumulations are found in the vicinity of the perforations with synchrotron tomography. Investigations with SEM and EDX analysis revealed the removal of PTFE in the perforated area and thereby a change to a hydrophilic surface. Thus, the water accumulation is proven to be correlated with the laser processing.

Acknowledgments

The authors like to thank H. Riesemeier (BAM Federal Institute for Material Research and Testing). Funding of the project PEM-CaD (grant number: 03SF0360B) by the Federal Ministry of Education and Research (BMBF) is gratefully acknowledged.

References

- [1] W. Vielstich, A. Lamm, H.A. Gasteiger, *Handbook of Fuel Cells – Fundamentals, Technology and Applications*, John Wiley & Sons, Chichester, 2003.
- [2] Z. Qi, A. Kaufman, *Journal of Power Sources* 109 (2002) 38–46.
- [3] J.T. Gostick, M.A. Ioannidis, M.W. Fowler, M.D. Pritzker, *Electrochemistry Communications* 11 (2009) 576–579.
- [4] C. Quick, D. Ritzinger, W. Lehnert, C. Hartnig, *Journal of Power Sources* 190 (2009) 110–120.
- [5] T. Kitahara, T. Konomi, H. Nakajima, *Journal of Power Sources* 195 (2010) 2202–2211.
- [6] Z. Lu, M.M. Daino, C. Rath, S.G. Kandlikar, *International Journal of Hydrogen Energy* 35 (2010) 4222–4233.
- [7] T. Sasabe, P. Deevanhxay, S. Tsushima, S. Hirai, *Electrochemistry Communications* 13 (2011) 638–641.
- [8] H. Markötter, I. Manke, P. Krüger, T. Arlt, J. Haußmann, M. Klages, H. Riesemeier, C. Hartnig, J. Scholte, J. Banhart, *Electrochemistry Communications* 13 (2011) 1001–1004.
- [9] S.D. Knights, K.M. Colbow, J. St-Pierre, D.P. Wilkinson, *Journal of Power Sources* 127 (2004) 127–134.
- [10] E.E. Kimball, J.B. Benziger, Y.G. Kevrekidis, *Fuel Cells* 10 (2010) 530–544.
- [11] K. Nishidaa, T. Murakamia, S. Tsushima, S. Hiraib, *Journal of Power Sources* 195 (2010) 3365–3373.
- [12] D. Gerteisen, T. Heilmann, C. Ziegler, *Journal of Power Sources* 177 (2008) 348–354.
- [13] D. Gerteisen, C. Sadeler, *Journal of Power Sources* 195 (2010) 5252–5257.
- [14] M.P. Manahan, M.C. Hatzell, E.C. Kumbur, M.M. Mench, *Journal of Power Sources* 196 (2011) 5573–5582.
- [15] M.P. Manahan, M.M. Mench, *ECS Transactions* 41 (2011) 569–581.
- [16] C. Hartnig, I. Manke, N. Kardjilov, A. Hilger, M. Grünerbel, J. Kaczorowski, J. Banhart, W. Lehnert, *Journal of Power Sources* 176 (2008) 452–459.
- [17] I. Manke, C. Hartnig, N. Kardjilov, M. Messerschmidt, A. Hilger, M. Strobl, W. Lehnert, J. Banhart, *Applied Physics Letters* 92 (2008) 244101.
- [18] I. Manke, C. Hartnig, M. Grünerbel, J. Kaczorowski, W. Lehnert, N. Kardjilov, A. Hilger, J. Banhart, W. Treimer, M. Strobl, *Applied Physics Letters* 90 (2007) 184101.
- [19] N. Kardjilov, I. Manke, A. Hilger, M. Strobl, J. Banhart, *Materials Today* 14 (2011) 248–256.
- [20] B. Schillinger, E. Lehmann, P. Vontobel, *Physica B: Condensed Matter* 276–278 (2000) 59–62.
- [21] R.J. Bellows, M.Y. Lin, M. Arif, A.K. Thompson, D. Jacobson, *Journal of the Electrochemical Society* 146 (1999) 1099–1103.
- [22] M.A. Hickner, N.P. Siegel, K.S. Chen, D.S. Hussey, D.L. Jacobson, M. Arif, *Journal of the Electrochemical Society* 155 (2008) B427–B434.
- [23] C. Tötzke, I. Manke, T. Arlt, H. Markötter, N. Kardjilov, A. Hilger, P. Krüger, C. Hartnig, J. Scholte, J. Banhart, *Journal of Power Sources* 196 (2011) 4631–4637.
- [24] E. Lehmann, *Pramana Journal of Physics* 71 (2008) 653–661.
- [25] S.H. Williams, A. Hilger, N. Kardjilov, I. Manke, M. Strobl, P.A. Douissard, T. Martin, H. Riesemeier, J. Banhart, *Journal of Instrumentation* 7 (2012) P02014.
- [26] R. Alink, D. Gerteisen, W. Mérida, *Fuel Cells* 11 (2011) 481–488.
- [27] H. Markötter, R. Alink, J. Haußmann, K. Dittmann, T. Arlt, F. Wieder, C. Tötzke, M. Klages, C. Reiter, H. Riesemeier, J. Scholte, D. Gerteisen, J. Banhart, I. Manke, *International Journal of Hydrogen Energy* 37 (2012) 7757–7761.
- [28] I. Manke, C. Hartnig, M. Grünerbel, W. Lehnert, N. Kardjilov, A. Haibel, A. Hilger, J. Banhart, H. Riesemeier, *Applied Physics Letters* 90 (2007) 1–3.
- [29] C. Hartnig, I. Manke, R. Kuhn, S. Kleinau, J. Goebels, J. Banhart, *Journal of Power Sources* 188 (2009) 468–474.
- [30] I. Manke, C. Hartnig, N. Kardjilov, H. Riesemeier, J. Goebels, R. Kuhn, P. Krüger, J. Banhart, *Fuel Cells* 10 (2010) 26–34.
- [31] T. Sasabe, P. Deevanhxay, S. Tsushima, S. Hirai, *Journal of Power Sources* 196 (2011) 8197–8206.
- [32] T. Sasabe, S. Tsushima, S. Hirai, *International Journal of Hydrogen Energy* 35 (2010) 11119–11128.
- [33] P. Deevanhxay, T. Sasabe, S. Tsushima, S. Hirai, *International Journal of Hydrogen Energy* 36 (2011) 10901–10907.
- [34] J. Kim, J. Je, T. Kim, M. Kaviani, S.Y. Son, M. Kim, *Current Applied Physics* 12 (2012) 105–108.
- [35] R. Kuhn, J. Scholte, P. Krüger, C. Hartnig, W. Lehnert, T. Arlt, I. Manke, *Journal of Power Sources* 196 (2011) 5231–5239.
- [36] P. Krüger, H. Markötter, J. Haußmann, M. Klages, T. Arlt, J. Banhart, C. Hartnig, I. Manke, J. Scholte, *Journal of Power Sources* 196 (2011) 5250–5255.
- [37] H. Markötter, I. Manke, J. Haußmann, T. Arlt, M. Klages, P. Krüger, C. Hartnig, J. Scholte, B.R. Müller, H. Riesemeier, J. Banhart, *Micro & Nano Letters* 7 (2012) 689–692.
- [38] Eller, *Journal of the Electrochemical Society* 158 (8) (2011) B963–B970.
- [39] E. Gülow, M. Schulze, N. Wagner, T. Kaz, R. Reissner, G. Steinhilber, A. Schneider, *Journal of Power Sources* 86 (2000) 352–362.
- [40] W. Görner, M.P. Hentschel, B.R. Müller, H. Riesemeier, M. Krumrey, G. Ulm, W. Dieter, U. Klein, R. Frahm, *Nuclear Instruments and Methods in Physics Research Section A: Accelerators, Spectrometers, Detectors and Associated Equipment* 467–468 (2001) S. 703–S. 706.
- [41] J. Roth, J. Eller, F.N. Büchi, *Journal of the Electrochemical Society* 159 (8) (2012) F449–F455.
- [42] A. Schneider, C. Wieser, J. Roth, L. Helfen, *Journal of Power Sources* 195 (2010) 6349–6355.
- [43] J. Banhart, A. Borbely, K. Dzieciol, F. Garcia-Moreno, I. Manke, N. Kardjilov, A.R. Kaysser-Pyzalla, M. Strobl, W. Treimer, *International Journal of Materials Research* 101 (2010) 1069–1079.
- [44] I. Manke, H. Markötter, C. Totzke, N. Kardjilov, R. Grothausmann, M. Dawson, C. Hartnig, S. Haas, D. Thomas, A. Hoell, C. Genzel, J. Banhart, *Advanced Engineering Materials* 13 (2011) 712–729.
- [45] H. Markötter, I. Manke, R. Kuhn, T. Arlt, N. Kardjilov, M.P. Hentschel, A. Kupsch, A. Lange, C. Hartnig, J. Scholte, J. Banhart, *Journal of Power Sources* 219 (2012) 120–125.